

# Seismic Facies Analysis: A Deep Domain Adaptation Approach

M Quamer Nasim<sup>1,2,\*</sup>, Tannistha Maiti<sup>1,3,\*</sup>, Ayush Shrivastava<sup>1,2</sup>, Tarry Singh<sup>1</sup>, and Jie Mei<sup>1,4</sup>

<sup>1</sup>deepkapha.ai, Amsterdam, Netherlands

<sup>2</sup>Indian Institute of Technology, Kharagpur, West Bengal, India

<sup>3</sup>University of Calgary, Canada

<sup>4</sup>University of Quebec at Trois-Rivieres, Canada

**Abstract**—Deep neural networks (DNNs) can learn accurately from large quantities of labeled input data, but DNNs sometimes fail to generalize to test data sampled from different input distributions. Unsupervised Deep Domain Adaptation (DDA) proves useful when no input labels are available, and distribution shifts are observed in the target domain (TD). Experiments are performed on seismic images of the F3 block 3D dataset from offshore Netherlands (source domain; SD) and Penobscot 3D survey data from Canada (target domain; TD). Three geological classes from SD and TD that have similar reflection patterns are considered. In the present study, an improved deep neural network architecture named EarthAdaptNet (EAN) is proposed to semantically segment the seismic images. We specifically use a transposed residual unit to replace the traditional dilated convolution in the decoder block. The EAN achieved a pixel-level accuracy >84% and an accuracy of ~70% for the minority classes, showing improved performance compared to existing architectures. In addition, we introduced the CORAL (Correlation Alignment) method to the EAN to create an unsupervised deep domain adaptation network (EAN-DDA) for the classification of seismic reflections from F3 and Penobscot. Maximum class accuracy achieved was ~99% for class 2 of Penobscot with >50% overall accuracy. Taken together, EAN-DDA has the potential to classify target domain seismic facies classes with high accuracy.

**Index Terms**—CORAL, Deep Learning, Domain Adaptation, EarthAdaptNet, Seismic Facies, Semantic Segmentation.

## 1. Introduction

INTERPRETATION of geologic features and inference of reservoir properties are key to the success of hydrocarbon exploration and production. Accurate delineation of subsurface structures is a necessary and routine process in seismic interpretation. Automation of this task will allow for timely delivery of interpreted seismic sections to support prospective zone identification, well planning, reservoir modeling, and geohazard analysis. In recent years, there is a massive interest in the application of DNNs for automating seismic interpretation[2-9].

Unfortunately, large publicly available annotated datasets for seismic interpretation are sparse, making the application of traditional deep learning methods challenging. To overcome this challenge, researchers often annotate their own training and testing datasets which is a time consuming process[2]. Few options to overcome scarcity in annotated data include a) weakly-supervised learning approaches [10], b) similarity-based data retrieval [1] and, c) weakly-supervised label mapping algorithm. Studies have also used unsupervised machine learning techniques such as principal component analysis or self-organizing maps[11-13]. Alternatively, researchers have proposed new architectures like Danet-FCN2 and Danet-FCN3 [14] that replaced the traditional dilated convolutions in the decoder block with a transposed residual unit thus reduced the amount of training data required.

The use of transfer learning with an already trained DNN can significantly reduce the costs associated with model training from scratch and leads to a high classification accuracy even with a smaller amount of training data[15]. To effectively apply knowledge acquired from one task to a different task in semantic classification, [16] used transfer learning and showed that a DNN trained with one seismic dataset could be reused in another similar task i.e., seismic facies semantic classification.[17] showed that trained DNN models would under-perform when tested on samples from a related, but non-identical domain by using transfer learning. However, transfer learning is still challenging in areas such as medical imaging and earth science because large annotated datasets are required for the models to benefit from the inductive transfer processes[18, 19].

Compared with natural image datasets, DDA for cross-modality images in earth science is more challenging. The existence of the domain shift is common in real-world applications[20, 21], where the semantic class labels are usually shared between domains while the distributions of data are different. For example, seismic images are acquired in different stratigraphic settings and are related by reflection patterns, stratigraphic settings, and depositional environments. These images differ due to modalities, such as stratigraphic settings and depositional environments. Data distributions of these modalities mismatch significantly, due to their different density, porosity, rock types, and permeability in the Earth (Figure 1).

To address this issue, unsupervised DDA methods have been proposed and evaluated to allow generalization of the trained models to new datasets[22]. The domain of labeled

---

\*Corresponding Authors: M Quamer Nasim, [quamer23nasim@yahoo.com](mailto:quamer23nasim@yahoo.com)  
Tannistha Maiti, [tannistha.maiti@deepkapha.ai](mailto:tannistha.maiti@deepkapha.ai)  
GitHub: <https://github.com/deepkapha/EarthAdaptNet>

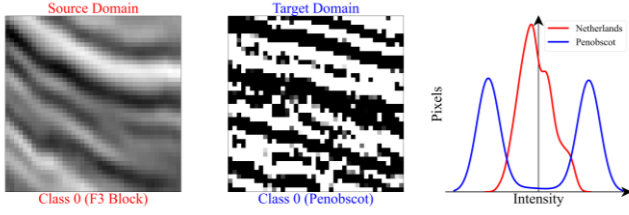


Figure 1. Domain Shift exists in seismic reflection pattern in terms of intensity and resolution (a) Reflection pattern of Class 1 Netherlands (b) Reflection pattern class 1 Penobscot (c) Histogram of Pixel intensity

training data is termed as the SD, and the test dataset is called the TD. The Unsupervised DDA methods are more feasible, given that these scenarios transfer knowledge across domains without using additional labels. To the best of our knowledge, how to enable effective generalization of trained DNNs across domains for seismic images has not been studied yet. Therefore, in this study, we try to focus on domain knowledge transfer between two different stratigraphic locations using reflection pattern similarities.

In this article, we present an approach that exploits accurate and robust semantic segmentation (classification) of seismic images with cropped local image patches on the F3 block of the Netherlands. We propose a network architecture with Residual Blocks (RBs) and Transposed Residual Blocks (TRBs) with skip connections between the two to address the issue of vanishing gradients. We also introduce the concept of DDA to bridge the gap between SD and TD in a joint space. The main contributions of this article are as follows.

- 1) We propose network architecture EarthAdaptNet for accurate delineation of seismic facies which is able to achieve higher performance in comparison to the baseline architecture. Here, we apply EAN architecture to classify seismic facies of the F3 block.
- 2) We redesign EarthAdaptNet to incorporate CORAL (Correlation Alignment for Domain Adaptation) method by constructing a differentiable loss function that minimizes the difference between source and target correlations, i.e., the CORAL loss, which learns the non-linear transformation between source and target correlations.
- 3) We assess performance of the proposed EAN-DDA in a multi-class classification problem to analyze seismic facies. The seismic facies dataset contains 3 representative facies classes that have similar depositional and compositional environments. We follow the standard protocol of domain adaptation [23] and use all labeled SD data and unlabeled TD data. We also generate patch images for the domain adaptation facies classification problem and make them publicly available.

The remainder of this article is organized as follows. Section 2 reviews network architectures and describes the proposed approach. Section 3 gives a detailed description of the background of DDA and application of CORAL method to EarthAdaptNet. Section 4 describes the datasets used in the semantic segmentation and steps to generate cropped patch

images for DDA analysis. The performance metrics used in this study are also presented in this section. Section 5 analyses the experimental results. Section 6 discusses on the results presented in this study. Section 7 draws the conclusions of this article and discusses future research directions.

## 2. Proposed Network Architectures

In the present study, we propose state-of-the-art architectures i.e., EarthAdaptNet and its variants, for semantic segmentation of seismic facies. We also present the EAN-DDA architecture for DDA of seismic facies.

### A. EarthAdaptNet

The architecture EarthAdaptNet (Figure 2) proposed for semantic segmentation is inspired by U-Net [24] and Danet-FCN3[14, 25]. Originally proposed for biomedical image segmentation, U-Net uses a contracting path to capture context and symmetrical expanding paths for attaining the original size of the input. Contracting and expanding paths are accompanied by shortcut connections at each level. Danet-FCN3 uses RBs and TRBs for semantic segmentation of seismic images. We therefore use U-Net to combine low level and high-level features [14] and Danet-FCN3 to overcome the issue of vanishing gradients[25, 26]. Building blocks of EarthAdaptNet can be broadly divided into RBs [26] and TRBs [25] similar to those of Danet-FCN3 but with some modifications. In the proposed architecture, RB comprises two convolutional layers, each followed by batch normalization and a downsampling residual connection of a 1X1 convolutional layer. In view of U-Net, this is what is referred to as the building block of the contracting path. TRB is similar in architecture to RB except with the use of a transposed convolutional layer instead of a convolutional layer. Upsampling transposed residual connection with a 1X1 convolutional layer is used instead of downsampling residual connection. EarthAdaptNet uses an Encoder-Decoder architecture with RBs and TRBs. The encoder starts with a convolutional layer and is followed by the RB, and the number of RBs used depends on the input size. In this study, we experimented with 3-5 RBs. The decoder starts with a TRB and the number of TRBs used is kept the same as the RB used in the Encoder. The transposed residual layer is followed by a transposed convolutional layer which outputs the segmented seismic image. A 1x1 convolutional layer also exists in the middle which acts as a bridge (bottleneck) between the Encoder and the Decoder. Skip connection is present between each RB and TRB.

We also introduced the atrous spatial pyramid pooling (ASPP) module from DeepLab V3 [27] in our EarthAdaptNet architecture in order to capture multi-scale features. ASPP module has 5 parallel layers, three of which are atrous convolutions of a 3X3 filter size with different dilatation rates (i.e., 6, 12, 18) and one 1X1 convolution layer and lastly, an image pooling layer. Each parallel layer in the ASPP module have 256 filters followed by a batch normalization layer. Finally, output of all 5 parallel layers is concatenated followed by another 1X1 convolution with 256 filters. With the help of 5 parallel layers and different atrous convolution rate, the

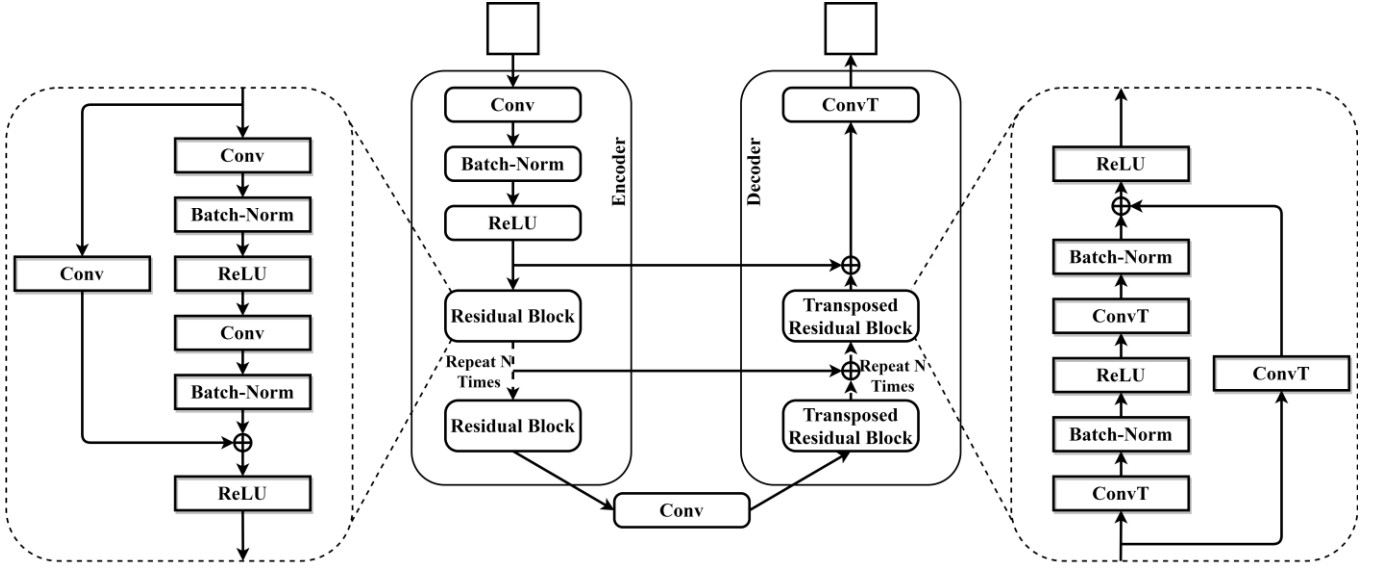


Figure 2. Building blocks of the proposed EarthAdaptNet, which consists of RBs and TRBs. RB comprises two convolutional (Conv) layers, each followed by batch normalization and a downsampling residual connection of the 1x1 Conv layer. TRB is similar in architecture as RB except with the use of a transposed convolutional (ConvT) layer instead of a convolutional layer. The encoder starts with a Conv Layer and is followed by the RB. Decoder starts with a TRB and the number of TRBs used is kept the same as the RB used in the Encoder and is followed by a Transposed Convolutional Layer which outputs the segmented seismic image. A 1x1 convolutional layer also exists in the middle which acts as a bridge (Bottleneck) between the Encoder and the Decoder. Skip connection is present between each RBs and TRBs.

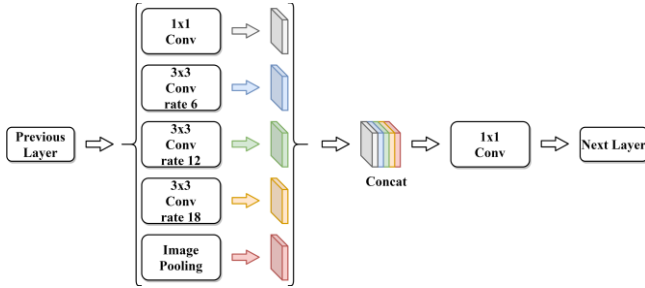


Figure 3. Atrous spatial pyramid pooling (ASPP) module having 5 parallel layers with three layers being 3x3 convolutional layers with dilatation rate of 6, 12, and 18. One layer being 1x1 convolutional layer and last layer being image pooling layer. Output of all of these 5 layers is concatenated followed by final 1x1 convolutional layer.

ASPP module is designed to capture multi-scale information (Figure 3).

Experiments were performed to examine the following architectures:

- 1) EarthAdaptNet model with a middle convolutional layer in 4 RB-TRB pairs;
- 2) EarthAdaptNet model with a middle convolutional layer in 5 RB-TRB pairs;
- 3) EarthAdaptNet model with a ASPP module in place of the middle convolutional layer in 4 RB-TRB pairs.

#### B. EarthAdaptNet domain adaptation network (EAN-DDA)

We revisited the EarthAdaptNet (EAN; Figure 4) and created three variations of this architecture, including:

- 1) 4 RBs followed by 4 fully connected layers ( $4RB + 4FC$ ; Table 1);
- 2) 4 RBs followed by Global Average Pooling (GAP) layer followed by 2 fully connected layers ( $4RB + GAP + 2FC$ ; Supplementary Table 1);

- 3) 3 RBs followed by Global Average Pooling layer followed by 2 fully connected layers ( $3RB + GAP + 2FC$ ; Supplementary Table 2).

Table 1, Supplementary Table 1 and Supplementary Table 2 show all the components for the respective architecture along with the size of the components.

The initial distribution of a random sample (batch size 128) is shown in Figure 7. As evident from the distribution plots based on [28], the source and target distributions differ greatly. Due to difference in data distribution, the performance of traditional deep learning approaches is compromised. Therefore, we introduced the EAN-DDA architecture based on DDA methodology which essentially bridges the gap between SD and TD. We discuss three variations of the EAN-DDA network with individually fine-tuned hyperparameters.

For the first variant of EAN-DDA model ( $4RB + 4FC$ ), we applied CORAL loss to all fully connected (FC) layers except the final output layer while for second ( $4RB + GAP + 2FC$ ) and third ( $3RB + GAP + 2FC$ ) variant, we applied GAP to flatten the results from the last encoder layer and then use CORAL loss to GAP layer and the 1<sup>st</sup> FC layer. It's a common practice to use GAP layer since it's a fairly simple operation that reduces the data significantly and prepares the model for the final classification module. We used CORAL loss with a weighting factor. Weighting factors in first variant ( $4RB + 4FC$ ) are 0.2, 0.6, and 0.2 for 1<sup>st</sup>, 2<sup>nd</sup>, and 3<sup>rd</sup> FC layers, respectively while for second ( $4RB + GAP + 2FC$ ) and third ( $3RB + GAP + 2FC$ ) variant weighting factors are 0.5 and 0.5 for the GAP and the 1<sup>st</sup> FC layers, respectively. In the third variant of EAN-DDA model ( $3RB + GAP + 2FC$ ) we decreased the number of RBs from 4 to 3 to see the model's performance, given that we're dealing with a patch size of 40X40 only.

We initialized the network parameters from a pre-trained network (Non-DDA Model) and fine-tuned it using the labeled

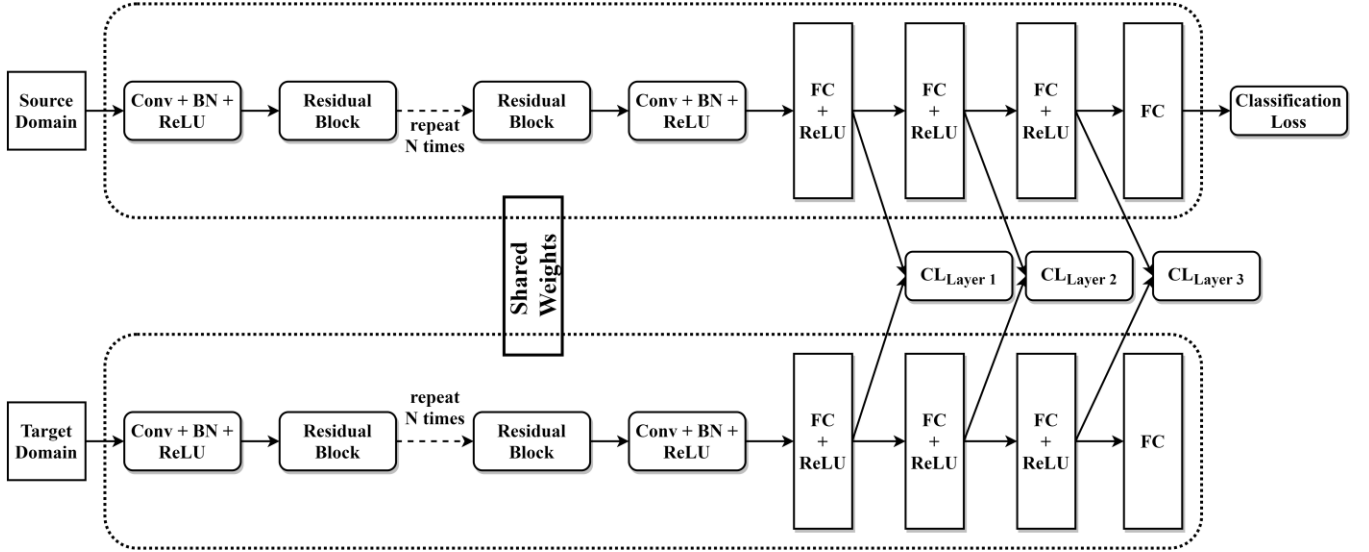


Figure 4. DeepCORAL architecture with the backbone of EarthAdaptNet's encoder which consists of RBs only. RBs are shown in Fig 2. We apply the CORAL loss to the three FC + ReLU layers and apply Classification loss to the last layer. Source: F3 cropped patch images, Target: Penobscot cropped patch images. SD and TD network shares common weights across the architecture

Table 1. Units Layerwise architectural description of the feature maps for the source and target domains for 4 encoders followed by 4 fc layers (4RB+4FC)

Entity	Entity Size	Entity Description
<i>first_conv_source</i>	(128, 64, 40, 40)	SD image batch feature map after first conv layer
<i>first_conv_target</i>	(128, 64, 40, 40)	TD image batch feature map after first conv layer
<i>rb_1_source</i>	(128, 64, 20, 20)	SD image batch feature map after first RB
<i>rb_1_target</i>	(128, 64, 20, 20)	TD image batch feature map after first RB
<i>rb_2_source</i>	(128, 128, 10, 10)	SD image batch feature map after second RB
<i>rb_2_target</i>	(128, 128, 10, 10)	TD image batch feature map after second RB
<i>rb_3_source</i>	(128, 256, 5, 5)	SD image batch feature map after third RB
<i>rb_3_target</i>	(128, 256, 5, 5)	TD image batch feature map after third RB
<i>rb_4_source</i>	(128, 512, 3, 3)	SD image batch feature map after fourth RB
<i>rb_4_target</i>	(128, 512, 3, 3)	TD image batch feature map after fourth RB
<i>last_conv_source</i>	(128, 512, 3, 3)	SD image batch feature map after last conv layer
<i>last_conv_target</i>	(128, 512, 3, 3)	TD image batch feature map after last conv layer
<i>fc1_source</i>	(128, 2048)	SD image batch feature map after first FC layer
<i>fc1_target</i>	(128, 2048)	TD image batch feature map after first FC layer
<i>fc2_source</i>	(128, 1024)	SD image batch feature map after second FC layer

SD data. The dimension of the last fully connected layer was set to the number of classes (i.e., 3), with weights initialized with  $N(0, 0.005)$  [23]. The learning rate of the last fully connected layer is set to 10 times the other layers as it was trained from scratch. The weight of the CORAL loss ( $\lambda$ ) is set in a way that at the end of the training the classification loss and CORAL loss are roughly the same [23].

### 3. Background on Domain Adaptation - EarthAdaptNet Unsupervised Domain Adaptation

In this study, we propose DDA method using the DeepCORAL (Correlation Alignment) [23] methodology for seismic facies classification, which uses CORAL Loss [23] to match the data distribution of the SD and TD at various feature layers. For this purpose, we first introduce CORAL loss for a single feature layer. Let us assume that we have SD

and TD  $d$ -dimensional encoded features from a particular feature layer as  $D_S$  and  $D_T$ , and the total amount of SD and TD data samples are  $n_S$  and  $n_T$ , respectively.  $D_S^{ij}$  ( $D_T^{ij}$ ) represents the  $j^{th}$  dimension of the  $i^{th}$  SD (TD) encoded feature for a particular feature layer and  $C_S$  ( $C_T$ ) denotes the feature covariance matrices. CORAL loss is defined as the distance between the second order statistics (covariances) of the SD and TD encoded features [23]:

$$l_{CORAL} = \frac{1}{4d^2} \|C_S - C_T\|_F^2 \quad (1)$$

Where  $\|\cdot\|_F^2$  represents the squared matrix Frobenius norm and can be calculated as follows. The covariance matrices of the SD and TD data are given by:

$$C_S = \frac{1}{n_S - 1} \left( D_S^T D_S - \frac{1}{n_S} (\mathbf{1}^T D_S)^T (\mathbf{1}^T D_S) \right) \quad (2)$$

$$C_T = \frac{1}{n_T - 1} \left( D_T^T D_T - \frac{1}{n_T} (\mathbf{1}^T D_T)^T (\mathbf{1}^T D_T) \right) \quad (3)$$



$$\|C_S - C_T\|_F^2 = \text{trace}((C_S - C_T)^*(C_S - C_T)) \quad (4)$$

Where  $\mathbf{1}$  in  $\mathbf{1}^T$  is a column vector with all elements equal to 1 and  $(C_S - C_T)^*$  is a conjugate transpose which can be computed as:

$$(C_S - C_T)^* = (\overline{C_S - C_T})^T \quad (5)$$

For the classification of seismic classes, we used a cross-entropy loss function. The CORAL loss is extended to total feature layers. By training the data on both classification and CORAL loss features are learned that work well on target domain.

$$l = l_{\text{CLASSIFICATION}} + \sum_{i=1}^t \lambda_i l_{\text{CORAL}} \quad (6)$$

where  $t$  denotes the number of CORAL loss layers in a deep neural network and  $\lambda$  represents the weight on each CORAL loss applied to  $t$  encoded feature layers. A difference between the ranges of classification loss and of CORAL loss was observed and a normalization factor is used to bring the two losses to comparable ranges.

## 4. Seismic Facies Dataset

### A. Dataset

In this study, we use processed seismic data from the F3 block, the Netherlands, Penobscot, and Canada datasets. Generating seismic images is a sophisticated process that involves data acquisition, where intense sound sources are placed between 6 and 76 m below the ground to generate sound waves. These waves pass through different layers of rock (strata) and are reflected, returning to the surface, where geophones or hydrophones can record them. This signal is then processed using an iterative procedure to generate seismic images. Finally, interpreters analyze the generated images and divide them into the different categories, or facies [29]. These categories represent the overall seismic characteristics rock unit that reflects its origin, differentiating this unit from the other ones around it [29]. It consists of a horizontal stack of 2D seismic images (slices), leading to a 3D volume, with the vertical axis of this volume representing its depth. The remaining axes define the inline and crossline directions. Geoscientists based their interpretations of facies based on configuration patterns that indicate geological factors like lithology, stratification, depositional systems, etc. [30].

In this work, we use publicly available dataset F3 Block, Netherlands 3D Survey ([https://github.com/olivesgatech/facies\\_classification\\_benchmark](https://github.com/olivesgatech/facies_classification_benchmark)). The inline slices are the images in the cube perpendicular to the inline direction. The same idea applies to the crossline slices, which are images along the depth axis and perpendicular to the crossline axis. The F3 dataset included 401 crossline and 701 inline slices, with a dimension of 401X701. In a previous study[2], the slices were interpreted and annotated, and a label mask was generated for each slice. F3 block seismic data consist of sections from inline 100 to 701 and crossline 300 to 1201. The training set contains the section from inline 300 to 700 and crossline 300 to 1000. Test set #1 contains a section from inline 100 to 299 and crossline 300 to 1000. Test set #2 contains a section from inline 100 to 700 and crossline 1001 to 1200. The main lithostratigraphic

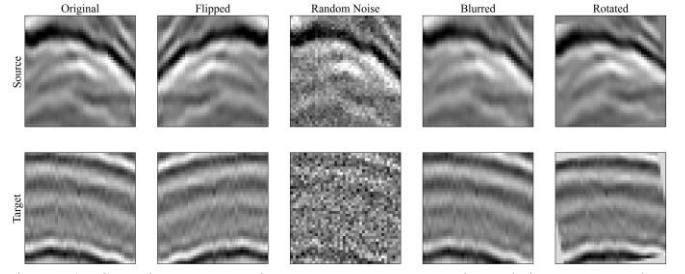


Figure 5. Sample augmentation to generate cropped patch images to solve DA classification problem; Source: F3 Block Target: Penobscot block. Original samples in (a) are flipped (b) random noise added, (c) blurred, and (d) rotated.

unit of the F3 block are the Upper North Sea group, the Lower and Middle North Sea group, Chalk group, Rijnland group, Schieland, Scruff and Niedersachsen groups, Altena group, Lower and Upper Germanic Trias groups, and Zechstein group, arranged according to their depth, with the Upper North Sea group representing shallowest horizon and Zechstein group representing deepest horizon.

We used another publicly available dataset of Penobscot, Canada 3D Survey (<https://zenodo.org/record/1324463#.X5cwFgzbIU>). This dataset is used in the present study as the TD. The Penobscot dataset included 481 crossline slices and 601 inline slices, with dimensions 601X1501 and 481X1501 pixels, respectively. All slices have been interpreted and annotated, and a label mask was generated per slice. The seven interpreted horizons: H1, H2, H3, H4, H5, H6, and H7[31] are numbered according to their depth, with H1 representing the deepest horizon and H7 representing the shallowest horizon.

### B. Representative Facies classes

Seismic stratigraphy [32], in conjunction with sequence stratigraphy [33], are two interpretation techniques developed to help predicting facies and reservoir distribution that add the time dimension to the depositional models [34]. Sequence stratigraphy is a complex model which is essentially based on sea-level changes and seismic stratigraphy is a technique that facilitates stratigraphic interpretation of seismic reflectors. Essentially, sequence stratigraphy applies the geological concepts of stratigraphy to the interpretation of seismic data. The basic assumption behind seismic stratigraphy is that individual reflectors can be considered as timelines, i.e., each represents a very short time interval of similar sedimentation conditions. This assumption signifies that a seismic reflector formed at different depositional environments and therefore it contains information of various lithofacies units. Seismic facies are classified based on reflection patterns including reflection configuration, reflection continuity, reflection amplitude and reflection terminations, based on which several geological interpretations could be made.

In this study, we have selected three representative facies classes from the F3 Netherlands block [2] and Penobscot data [35]. The representative facies were selected based on their lithofacies composition, depositional environment and reflection patterns (Table 2). The comparable facies classes from F3 and Penobscot are renamed as Class 1, Class 2 and Class 3 respectively based on similar reflection pattern and are used for comparison in DA studies. The depositional

Table 2. Interpreted horizons of Netherlands F3 block and Canada Penobscot data. Comparisons are made based on Composition and Depositional environment and reflection patterns. Representative classes are the class names used in DA studies

Formation	Compositional and Depositional Environment	Reflection Pattern	Representative Class
Chalk and Rijnland	Clay Formations with Sandstones; Coastal shallow to fairly deep open Marine environment	Parallel and High-Amplitude Reflectors	Class 1
Scuff	Claystones; Shallow Marine to continental Marine environment from restricted(lagoonal) to open Marine (outer shelf) condition	Subparallel and Varying-Amplitude Reflectors	Class 2
Zechstein	Evaporites and Carbonates; Peri Marine to Marine settings	Continuous and Very Low-Amplitude Reflectors with very minor apparent reflections	Class 3
H6-H5	Carbonates and Clastics of Iroquois Formation and Coarse Clastic Fluvial sediments of Mohican Formation; Shallow Marine setting	Parallel, Chaotic and High-Amplitude Reflectors	Class 1
H5-H4	Fine-grained Glaciomarine, Gravel, 3-41% Sand, 30-56% Silt, and 29-45% Clay; Marine transgression, Reflectors having Prograding Sigmoidal Configuration of Low Energy And Medium to Low Amplitude due To Complex Delta System Deposition	Subparallel and Varying-Amplitude Reflectors	Class 2
H4-H3	Coastal area having a complex history of glaciation and sea-level rise	Continuous and Low-Amplitude Reflectors	Class 3

environment for the F3 block is predominantly shallow marine-to-marine depositions along with restricted marine and floodplain settings, while the Penobscot block has marine water filled basins.

### C. Generate patches from the dataset

The patch-based model for segmentation problem extracts 2-D patches of a given size from the seismic sections i.e., inline and crossline sections which itself is extracted from seismic volume along with their masks[2]. We have used patches of the dimension 99X99. The stride is set to half the size of the patch. A window of a given size (patch size) moves all over a section, whose  $i^{th}$  pixel is apart from the  $i^{th}$  pixel of adjacent window by half the value of given patch size. Once all the patches were extracted using the above-mentioned method, 20% of them were kept aside to use for validation set.

To approach the classification problem, we generated a patch size of 40X40 from both SD (the Netherlands) and TD (Canada). A single-valued label indicating the facies class is then assigned to each patch, and if 70% or more pixels of a patch belong to a particular class, we assign the corresponding single-valued class label to that patch. If less than 70% of all pixels of a patch belong to a particular class, the patch was excluded.

### D. Data Augmentation

Data augmentation enables practitioners to significantly increase the diversity of data available for training deep learning models without the need to collect new data. Figure 5 illustrates the augmentations applied to the cropped patches, including random rotation ( $\leq 10$  degrees), blurring, flipping, shifting, and adding random noises.[2]. Previous studies [2] showed that data augmentation significantly improved the performance of both baseline models, i.e., patch-based model and section based model, but the effect was more pronounced for the patch-based model. [2] found that the frequency weighted intersection over union (FWIoU) and mean class accuracy (MCA) scores increased by more than 10% in the patch-based model, while model performance was improved more significantly on smaller classes such as the Zechstein and Scuff groups.

### E. Model Training

We performed several experiments with mini-batch sizes between 32 and 16. Tests were performed using the Adam and AdaDelta optimizers with different learning rates (i.e.,  $10^{-1}$ ,  $10^{-2}$ ,  $10^{-3}$ , and  $10^{-5}$ ) and a maximum number of epochs of 50. The learning rates were kept constant for the entire training process. A dropout of 0.5 was also used. AdaDelta was used for EAN with ASPP module while Adam was used for other architectures. We used a weight decay parameter of 0.0001 for both Adam and AdaDelta optimizers while all other parameters were set to the default values. We trained the models with PyTorch 1.5.1 on Google Colaboratory using a 12GB NVIDIA Tesla K80 GPU.

### F. Evaluation Metrics

Several evaluation metrics for segmentation and classification derived from the confusion matrix were used to measure the performance of the proposed model.

1) *Segmentation*: To evaluate model performance, we used metrics including pixel accuracy (PA), class accuracy (CA), mean class accuracy (MCA), intersection over union (IoU), mean IoU (MIoU) and frequency weighted IoU (FWIoU), which are all commonly used metrics in the evaluation of computer vision models.  $G_i$  represents the ground truth of pixels for class  $i$ ,  $P_i$  represents prediction for the class  $i$  and  $n_c$  represents the total number of the classes present. Metrics used in the present study are defined as follows:

a) **Pixel accuracy (PA)** is the percentage of total pixels correctly classified.

$$PA = \frac{\sum_i |P_i \cap G_i|}{\sum_i G_i} \quad (7)$$

b) **Class accuracy (CA)** is the percentage of total pixels correctly predicted for a particular class. We also used **mean class accuracy (MCA)** which is the average of CA.

$$CA = \frac{|P_i \cap G_i|}{G_i} \quad (8)$$

$$MCA = \frac{1}{n_c} \sum_i CA_i \quad (9)$$

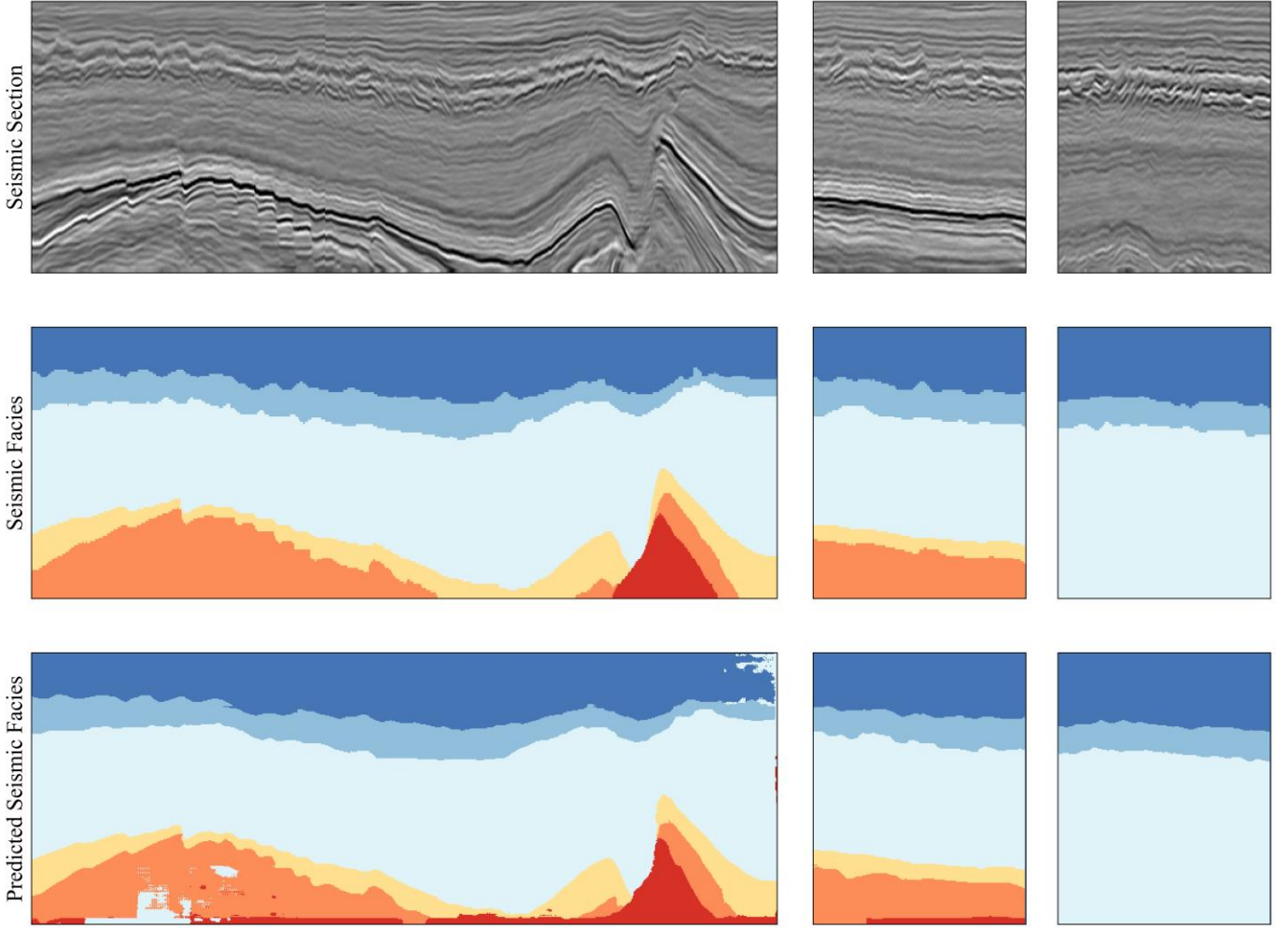


Figure 6. Top section: raw seismic section along inlines 295, crossline 620 from #Test1 and crossline 411 from #Test2 respectively. Middle section: Original labels and bottom section: Interpreted labels from 4 RB-TRB pairs with ASPP model

c) **Intersection over union (IoU)**, also known as the **Jaccard Index**, is a measure of overlap between the predicted masks and the true masks. We also used **mean IoU (MIOU)**, calculated by averaging the IoU overall classes. IoU can be reformulated as the number of true positives (intersection) over the sum of true positives and false negatives. The metrics gives an estimate of how well the (x, y)-coordinates of our predicted bounding box is going to exactly match the (x, y)-coordinates of the ground-truth bounding box. Since the present dataset is of class imbalance, we weighed each class by its size, giving us the **frequency weighted IoU (FWIoU)**.

$$IoU_i = \frac{|P_i \cap G_i|}{|P_i \cup G_i|} \quad (10)$$

$$MIOU = \frac{1}{n_c} \sum_i IoU_i \quad (11)$$

$$FWIoU = \frac{1}{\sum_i G_i} \cdot \sum_i |G_i| \cdot \frac{|P_i \cap G_i|}{|P_i \cup G_i|} \quad (12)$$

2) **Domain Adaptation**: The confusion matrix is used to calculate the number or frequency of true positive (TP), true negative (TN), false positive (FP), and false negative (FN). Results of DDA are evaluated using the following metrics:

a) **Class accuracy (CA)** measures how often the model predicts each class correctly. We also use **mean CA (MCA)** to save the checkpoints of our model. CA and MCA derived from the confusion matrix are calculated using the following equations:

$$CA = \frac{TP + TN}{TP + FP + TN + FN} \quad (13)$$

$$MCA = \frac{1}{n_c} \sum_i CA_i \quad (14)$$

b) **Precision** is a measure of the exactness of a model as it tells us that if a positive value is predicted by a model, how often is that prediction correct:

$$Precision = \frac{TP}{TP + FP} \quad (15)$$

c) **Recall**, also known as **true positive rate (TPR)** or **sensitivity**, is a measure of the completeness of positive

Table 3. Results of EarthAdaptNet with its variation models when tested on both test splits of the dataset. All metrics are in the range (0-1) with larger values being better. All the metrics that have outperformed baseline model [2] are in bold numbers. In baseline model, MIoU wasn't reported hence the bold MIoU represents best performing model.

Architecture	PA	MCA	FWIoU	MIoU	CA					
					1	2	3	4	5	6
5 RB-TRB Pairs	0.82	<b>0.76</b>	0.73	0.60	0.91	0.86	0.96	<b>0.70</b>	0.24	<b>0.86</b>
4 RB-TRB Pairs	0.85	0.69	0.74	0.57	0.96	0.83	0.94	<b>0.70</b>	<b>0.31</b>	0.39
4 RB-TRB Pairs + ASPP	0.85	<b>0.78</b>	<b>0.77</b>	<b>0.62</b>	0.95	0.84	0.94	<b>0.73</b>	<b>0.35</b>	<b>0.84</b>

outcomes of a model and it tells us that if the actual value is positive, how often the prediction is correct:

$$Recall = \frac{TP}{TP + FN} \quad (16)$$

d) **F1 Score** is the harmonic mean of precision and recall:

$$F1\ Score = \frac{Precision * Recall}{Precision + Recall} \quad (17)$$

e) **Pearson coefficient** ( $r_p$ ) is well-known to researchers for the standard scenario of normally distributed variables.  $r_p$  or bivariate correlation measures linear correlation between two variables X and Y for finite sample sizes [36]. Correlation is a bivariate analysis that measures the strength of association between two variables and the direction of their relationship. In terms of the strength of relationship, the value of the correlation coefficient varies between +1 and -1. A value of  $\pm 1$  indicates a perfect degree of association between the two variables. As the correlation coefficient value goes towards 0, the relationship between the two variables will be weaker. The direction of the relationship is indicated by the sign of the coefficient; a + sign indicates a positive relationship and a - sign indicates a negative relationship.

f) **p - value** is used to estimate the linear relationship between two variables. In this study, a *p - value* < 0.05 refers to statistically significant difference and *p* > 0.05 means no statistically significant difference.

## 5. Experimental Results

### A. Segmentation

EarthAdaptNet achieves an accuracy of >80% when applied to the 3 classes that belongs to the North Sea Group (Table 3). As shown in Table 3, *4 RB-TRB Pairs with ASPP* and *5 RB-TRB Pairs* were able to give an overall accuracy of ~85% for the Zechstein class. This is a substantial improvement in comparison to performance of the baseline model used in one previous study[2]. Although *4RB-TRB Pairs* was unable to capture the last 2 classes with comparable accuracy, with the introduction of an ASPP module, it has shown improved performance on those 2 classes as well. The results we present prove that our model is able to capture the last 3 classes which was otherwise not possible using the baseline model. The segmentation results are shown in Figure 6. For the few pixels for the section inline 295 and crossline 620, misclassification occurred as the model was not able to efficiently identify scruff for the North Sea groups.

Table 4. Mean Class Accuracy shifts between Netherlands and Canada. N\_Class  $\rightarrow$  C\_Class defines the shift from the facies class from Netherlands to Canada

Experiment	N_1 $\rightarrow$ C_1	N_2 $\rightarrow$ C_2	N_3 $\rightarrow$ C_3
Direct Test	0.40	0.58	0.15
3RB+GAP+2FC	0.56	0.67	0.04
4RB+GAP+2FC	0.88	0.66	0.01
4RB+4FC	0.82	0.99	0.16

### B. Deep Domain Adaptation

Experimental results obtained from the 3 DDA models are listed in Table 4, which demonstrate that the proposed unsupervised domain adaptation method effectively maps the feature space of TD (Canada) to that of SD (the Netherlands). This study is a first of a kind application of DDA to the seismic facies classification. To experimentally explore the potential upper bounds of the classification accuracy, we implemented three different model variants (Table 1, Supplementary Table 1, and Supplementary Table 2). To address the severe domain shift problem in seismic image analysis, we applied a classifier trained on the Netherlands domain to the Canada domain through a “direct test”, which is defined as a scenario where the weights of a model trained on the Netherlands F3 data are directly used to predict labels for the Penobscot dataset. The model that achieves the best performance on the direct test completely failed on Canada data, with a maximum accuracy of 0.40, 0.58, and 0.15 respectively for the three classes. This leads to the conclusion that although reflection patterns from the Netherlands and Canada are similar, i.e., sharing high level representations and identical label space, the significant difference in their low-level characteristics makes it extremely difficult for models trained on the Netherlands data to effectively extract features from the Canada data.

With our unsupervised DDA method, we observe a great improvement in the classification performance on the TD (Canada) compared with that achieved by the direct test on the TD (Canada). More specifically, the EAN-DDA model has increased the average accuracy of ~40% to 50% for facies classes in Canada. Class H5-H4 of Canada can be correlated best with the Scuff group of the Netherlands and is detected with 99% accuracy, resulting in an increase in accuracy of 33% from the direct test. Class H6-H5 of Canada can be correlated best with the Chalk and Rijnland group of the Netherlands and is detected with 82% accuracy, indicating an increase in accuracy of 42% from the direct test. Class H4-H3 of Canada can be correlated best with the Zeichstien group of the Netherlands and is detected with 16% accuracy, showing an



Table 5. Statistical variants for 4RB+4FC architecture. Pearson coefficient and p-value determine how well DDA model perform.

Entity	Pearson Coefficient	p-value
<i>first_conv_source - first_conv_target</i>	0.15	0.00
<i>rb_1_source - rb_1_target</i>	0.37	0.00
<i>rb_2_source - rb_2_target</i>	0.43	0.00
<i>rb_3_source - rb_3_target</i>	0.49	0.18
<i>rb_4_source - rb_4_target</i>	0.36	0.83
<i>fc1_source - fc1_target</i>	0.36	0.94
<i>fc2_source - fc2_target</i>	0.33	0.01
<i>fc3_source - fc3_target</i>	0.26	0.00

increase in accuracy of 1% compared with the direct test. Reflection pattern of Zechstien and H4-H3 doesn't match properly (Table 2), making the EAN-DDA model unable to achieve good performance for class 3. Given that the goal of the DDA method is to map SD and TD to a domain invariant feature space, we have successfully matched the distributions of SD and TD across the networks (Figure 8, Supplementary Figure 1, Supplementary Figure 2). The  $r_p$  and  $p$ -value between feature maps of SD and TD are reported in Table 5, Supplementary Table 3, and Supplementary Table 4.

## 6. Discussion

### A. Optimizer Selection

To perform a comparison between the models tested, a mini-batch size of 32 is used. We store the model weights for best performing epoch and the definition of best performing model was set to track the best MCA achieved. Experiments are performed primarily to analyze the behavior of different optimizers including Adam and AdaDelta, and as mentioned in section 4D, to fine tune the decay parameter. Adadelta and Adam are very similar algorithms that perform comparably well in similar circumstances. However, based on [37], we infer that the bias-correction in the Adam optimizer slightly outperforms towards the end of the optimization process as gradients become sparser. Hence, Adam has been suggested to be a better overall choice over Adadelta [38]. The second set of experiments was performed to determine an epoch size, so the model training does not reach timeout. The models were tested for 50 and 100 epochs respectively, where we did not observe a significant increase in CA (~2%) of the North Sea group.

### B. Patch-based models

The model architectures used in this study are patch-based, i.e., trained on patches from different depths, since the spatial dependencies are lost the architectures which led to confusion between facies classes. Section based models are superior to patch-based models due to their ability to incorporate spatial and contextual information within each seismic section. However, because of the unknown size of the sections, the computations can become very slow.

In this study, it is observed that the Scruff group is mostly confused with the Lower North Sea group [2]. Due to class imbalance in the F3 dataset, the architecture is trained on far more examples of the Lower or Upper North Sea groups than that of the Zechstein or Scruff groups. This makes the networks biased towards classifying pixels as the Lower or Upper North Sea groups and therefore artificially achieving

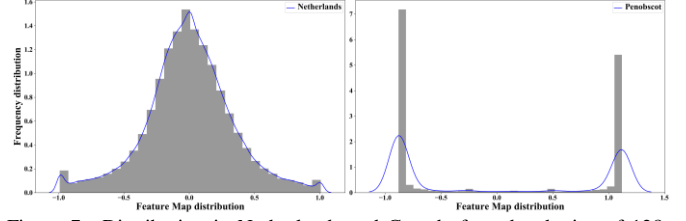


Figure 7. Distribution in Netherlands and Canada for a batch size of 128. This batch is used to generate the feature map for the three variants of the DA model discussed. The initial distribution for Netherlands and Canada is significantly different. CORAL loss applies a non-linear transformation between TD and SD and the final classification result for TD has good accuracy.

higher class accuracy scores for those classes. In addition, the majority classes have a more diverse visual appearance compared to the minority classes and therefore, the network may confuse features learned from the minority classes with those learned from the majority classes. Nevertheless, using techniques such as data augmentation, we overcome the problem of class imbalance and the accuracy for classifying the minority classes, such as the Zechstein and Scruff groups, improved by 17% and 14.7% [2].

In comparison to the patch-based baseline model [2], EAN converges faster when the same data loader is used. For classes 1, 4, 5 and 6, the EAN outperformed the baseline model by 2%, 6%, 6%, and 38%, respectively, as measured by accuracy.

### C. Encoder - Decoder Architecture

EarthAdaptNet uses RBs [25] to extract features (encoder) and transposed units of the same structure to reconstruct the original image with its respective labels (decoder). The skip connections skip some layers in the neural network and feed the output of one given layer as the input to the next few layers, instead of only the next immediate layer. It provides an alternative path for the gradient (with backpropagation) to flow through the network, and these additional paths are beneficial for the convergence of models during training. The skip connection incorporates the topology to combine coarse information with detailed, lower layer information. In the present study, the 4 RBs architecture has a downsampled image size of 7X7 whereas the 5 RBs architecture has a downsampled image size of 3X3. Hence the 4 RBs architecture has access to more samples, which eventually leads to a higher MCA.

The 4 RBs with ASPP achieve a better performance with an MCA of 78%, and a Mean IoU of 62% which shows that the spatial coordinates are predicted slightly more accurately and the ASPP greatly enlarges the Valid Receptive Field (VRF). However, due to the cropping size, the VRF field is also limited to local patches, where not enough context information is included. The downscaled images used in the first training stage greatly enlarge the VRF. VRF is known to be crucial for the image-based classification of objects [39], and if the VRF is large enough to represent the whole object and its surroundings, a DNN architecture learns the potential representations of their correlations more efficiently [39]. The proposed architecture was able to give a MCA of ~85% for the Zechstein class.

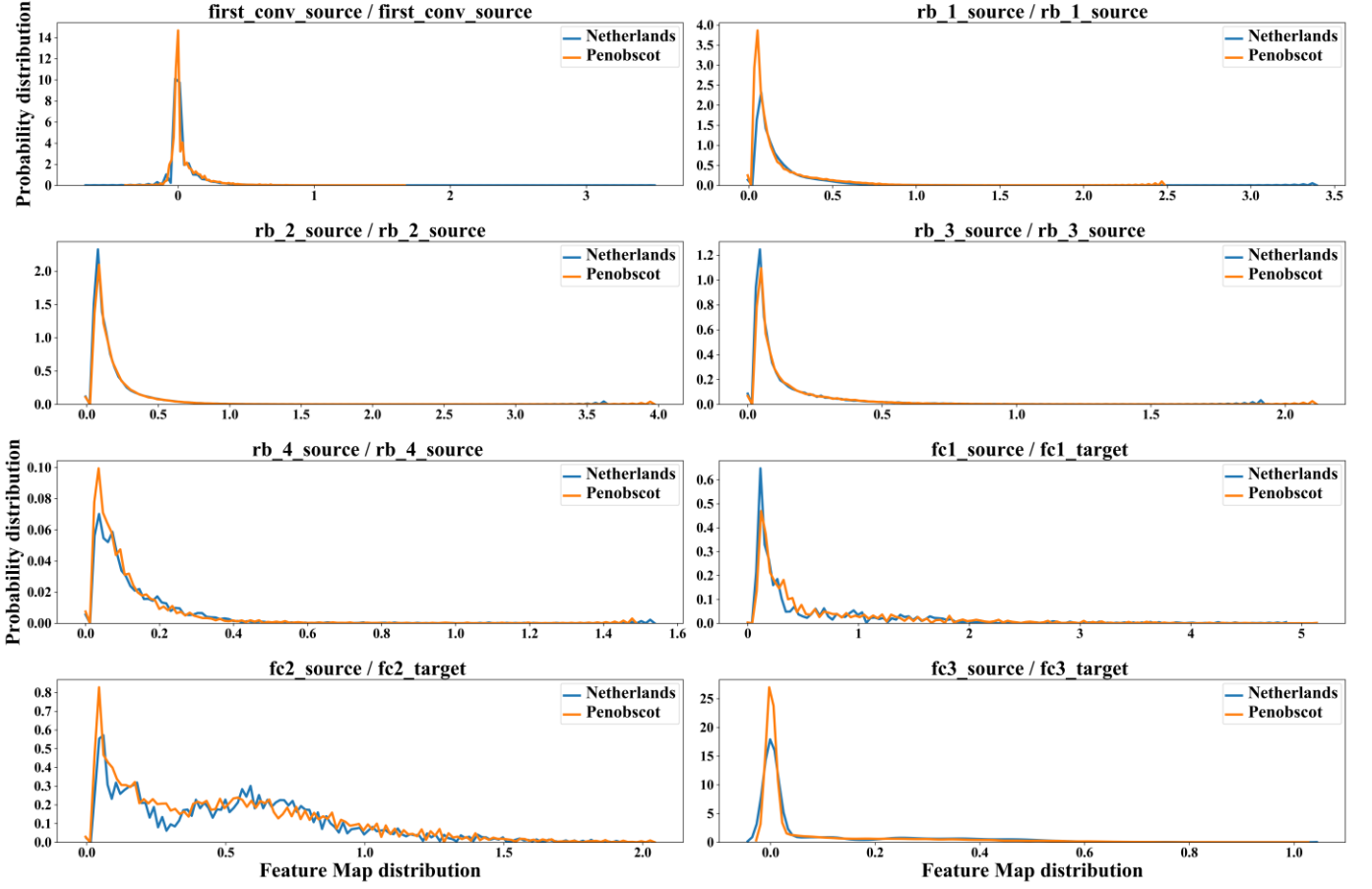


Figure 8. Comparison of the feature maps distributions from source and target domains. Distributions from the layer for the architecture with 4 Encoders followed by 4 FC layers ( $4RB+4FC$ ) shows how the SD (Netherlands) and TD (Canada) distributions correlate.

#### D. Distribution of feature maps

To study the performance of the EAN-DDA architecture and how its various components affect the accuracy of the classification of each class, we plot the probability distribution of feature maps. To measure the similarity among feature maps, a batch size of 128 was randomly selected and feature maps were generated for all the three models viz:  $4RB+4FC$ ,  $4RB+GAP+2FC$  and  $3RB+GAP+2FC$ . The similarity of the feature map distributions is calculated using the Pearson coefficient  $r_p$  and  $p$ -value.

Figure 8 shows the distribution of feature maps of the  $4RB+4FC$  architecture after training for 100 epochs. The similarity improves in deeper layers as indicated by the  $r_p$  values. Furthermore, a  $p$ -value  $> 0.05$  shows that the similarity of distributions is statistically significant (Table 5). The  $r_p$  value for first three fully connected layers is positive, indicating the features from source and target correlate. We can clearly see that adding the CORAL loss helps achieve better performance on the target domain while maintaining strong classification accuracy on the source domain [23].

Supplementary Figure 1 shows the distribution of output feature maps for the  $4RB+GAP+2FC$  architecture after training for 100 epochs. Based on Supplementary Table 3, the output feature map from the first and the second encoders are not well correlated as indicated by the low  $r_p$  values. While the feature maps of deeper layers start getting similar, the

distribution of  $rb_2\_source - rb_2\_target$  has a higher  $r_p$  value than that of the  $3RB+GAP+2FC$  architecture. The  $rb_3\_source - rb_3\_target$  has higher  $r_p$  in comparison to other deeper layers i.e.,  $rb_4\_source - rb_4\_target$ . However, the  $p$ -value for all the distributions is  $< 0.05$  hence the source-target distributions are not statistically significant. Again, the distribution of  $fc1\_source - fc1\_target$  deviates from a regular bell curve so the  $r_p$  value might be inconclusive.

Supplementary Figure 2 shows the distribution of output feature maps for the  $3RB+GAP+2FC$  architecture after training for 100 epochs. Based on Supplementary Table 4, the output feature map from the first encoder and the second encoder are not well correlated, indicated by  $r_p$  values of 0.02 and 0.00 respectively. The highest  $r_p$  value is observed from  $rb_3\_source - rb_3\_target$  as feature maps in deeper layers start getting more similar. However, the  $p$ -value for all the distribution is  $< 0.05$  hence the source-target distributions are not statistically significant. The distribution from  $rb_3\_source - rb_3\_target$  deviates from a regular bell curve and the  $r_p$  value is inconclusive.

#### E. Effect of Global Average Pooling

GAP is an operation that calculates the average output of feature maps in the previous layer. This operation reduces the data load significantly and prepares the model for the final classification layer. Since GAP does not contain anything trainable, the  $r_p$  between the source and target might not be

well correlated as shown in models  $4RB+GAP+2FC$  and  $3RB+GAP+2FC$ .

## 7. Conclusion

In conclusion, we have introduced a deep learning model EarthAdaptNet that can efficiently classify facies with patch sections and is able to achieve a classification accuracy  $>50\%$  for smaller classes like Zechstein and Scruff. The architecture performs better than the patch-based baseline model. We present and describe an effective and efficient method for unsupervised domain adaptation using the CORrelation ALIGNment (CORAL) method. The CORAL method minimizes domain shift by aligning the second-order statistics of source and target distributions, without requiring any target labels. The CORAL loss applied to domain adaptation algorithms is then extended to EarthAdaptNet. The proposed DDA approach is among one of the first applications of DDA to the study for unlabeled seismic facies, and as a result, two out of the three classes of Penobscot were classified with an accuracy  $>80\%$ . We also present and examine 3 variants of the proposed DDA architecture to understand how the components such as residual blocks, global average pooling and fully connected layers behave in domain adaptation. We note that the  $4RB+4FCDDA$  model shows promising results on class 1 and class 2. We observe that more complex classifier modules (i.e., classifier modules with greater number of FC layers) lead to higher accuracy, as the MCA of  $4RB+4FC$  is  $\sim 66\%$  while the MCA of  $4RB+GAP+2FC$  is  $\sim 52\%$ . In the meantime, accuracy decreased with decrease in the number of RBs used in the contracting path: the MCA of  $3RB+GAP+2FC$  is  $\sim 42\%$  which is the lowest among all the three EAN-DDA models variants. Domain transfer for class 3 of SD to TD is not efficient, since the reflection pattern of the Zechstein group of SD doesn't exactly match with that of the H4-H3 of TD. The average MCA of all presented EAN-DDA models is  $\sim 53\%$ . The feature map distribution study of SD and TD is proved useful to verify how well the target domain is adapting.

One limitation of patch-based models for segmentation is that the model doesn't get to see the whole seismic section at a time, instead, it only looks at a patch and loses spatial information. To overcome these difficulties in the patch-based model we propose (1) metadata tagging and (2) the use of architecture like Recurrent Neural Networks to preserve the spatial information. As seismic data is essentially a time series data it already incorporates spatial information.

The present study apply DDA methods to the seismic reflection patterns. The study can be potentially extended to validate and understand the generalizability of the proposed approach to different geological domains. Deep Domain Adaptation can be used to study other seismic attributes such as Direct Hydrocarbon Indicators (DHIs) like bright spot from seismic data and hydrocarbon detection from well logs. Future research directions will include (1) conversion of classification problem to segmentation problem (2) EAN-DDA study is a Divergence-based DDA methodology which specifically is designed for classification. For segmentation, one can use Adversarial-based DDA such as CoGAN[40] and Pixel-level Domain Transfer[41].

## Acknowledgment

This research was supported and funded by [LiveAI](#). The facilities of F3 seismic Data Services were accessed from [olivesgatech](#) GitHub handle and for Penobscot data from [zenodo.org](#) by [Baroni 2018](#). Data for F3 and Penobscot are freely available for research purpose. We thank Md Rifat Arefin for providing comments and suggestions on model training.

## References

- [1] Alaudah, Y., S. Gao, and G. AlRegib, *Learning to label seismic structures with deconvolution networks and weak labels*, in *SEG Technical Program Expanded Abstracts 2018*. 2018, Society of Exploration Geophysicists. p. 2121-2125.
- [2] Alaudah, Y., et al., *A machine-learning benchmark for facies classification*. Interpretation, 2019. **7**(3): p. SE175-SE187.
- [3] Di, H., Z. Wang, and G. AlRegib, *Real-time seismic-image interpretation via deconvolutional neural network*, in *SEG Technical Program Expanded Abstracts 2018*. 2018, Society of Exploration Geophysicists. p. 2051-2055.
- [4] Dramsch, J.S. and M. L  thje, *Deep-learning seismic facies on state-of-the-art CNN architectures*, in *SEG Technical Program Expanded Abstracts 2018*. 2018, Society of Exploration Geophysicists. p. 2036-2040.
- [5] Huang, L., X. Dong, and T.E. Clee, *A scalable deep learning platform for identifying geologic features from seismic attributes*. The Leading Edge, 2017. **36**(3): p. 249-256.
- [6] Shi, Y., X. Wu, and S. Fomel, *Automatic salt-body classification using a deep convolutional neural network*, in *SEG Technical Program Expanded Abstracts 2018*. 2018, Society of Exploration Geophysicists. p. 1971-1975.
- [7] Waldehand, A.U. and A. Solberg, *Salt classification using deep learning*. European Association of Geoscientists & Engineers.
- [8] Zhao, T., *Seismic facies classification using different deep convolutional neural networks*, in *SEG Technical Program Expanded Abstracts 2018*. 2018, Society of Exploration Geophysicists. p. 2046-2050.
- [9] Araya-Polo, M., et al., *Automated fault detection without seismic processing*. The Leading Edge, 2017. **36**(3): p. 208-214.
- [10] Alaudah, Y. and G. AlRegib, *Weakly-supervised labeling of seismic volumes using reference exemplars*. IEEE.
- [11] Col  ou, T., M. Poupon, and K. Azbel, *Unsupervised seismic facies classification: A review and comparison of techniques and implementation*. The Leading Edge, 2003. **22**(10): p. 942-953.
- [12] de Matos, M.C., P.L. Osorio, and P.R. Johann, *Unsupervised seismic facies analysis using wavelet transform and self-organizing maps*. Geophysics, 2007. **72**(1): p. P9-P21.
- [13] Dubois, M.K., G.C. Bohling, and S. Chakrabarti, *Comparison of four approaches to a rock facies classification problem*. Computers & Geosciences, 2007. **33**(5): p. 599-617.
- [14] Civitarese, D., et al., *Semantic segmentation of seismic images*. arXiv preprint arXiv:1905.04307, 2019.
- [15] Hagos, M.T. and S. Kant, *Transfer learning based detection of diabetic retinopathy from small dataset*. arXiv preprint arXiv:1905.07203, 2019.
- [16] Chevotarese, D., et al., *Transfer learning applied to seismic images classification*. AAPG Annual and Exhibition, 2018.
- [17] Dou, Q., et al., *Unsupervised cross-modality domain adaptation of convnets for biomedical image segmentations with adversarial loss*. arXiv preprint arXiv:1804.10916, 2018.
- [18] Yosinski, J., et al. *How transferable are features in deep neural networks?*
- [19] Zamir, A.R., et al. *Taskonomy: Disentangling task transfer learning*.
- [20] Gretton, A., et al., *Covariate shift by kernel mean matching*. Dataset shift in machine learning, 2009. **3**(4): p. 5.
- [21] Torralba, A. and A.A. Efros. *Unbiased look at dataset bias*. IEEE.
- [22] Patel, V.M., et al., *Visual domain adaptation: A survey of recent advances*. IEEE signal processing magazine, 2015. **32**(3): p. 53-69.

- [23] Sun, B. and K. Saenko. *Deep coral: Correlation alignment for deep domain adaptation*. 2016. Springer.
- [24] Ronneberger, O., P. Fischer, and T. Brox. *U-net: Convolutional networks for biomedical image segmentation*. Springer.
- [25] He, K., et al. *Deep residual learning for image recognition*.
- [26] Wojna, Z., et al., *The devil is in the decoder: Classification, regression and gans*. International Journal of Computer Vision, 2019. **127**(11-12): p. 1694-1706.
- [27] Chen, L.-C., et al., *Rethinking atrous convolution for semantic image segmentation*. arXiv preprint arXiv:1706.05587, 2017.
- [28] Zhao, Q., et al., *Interpretable Relative Squeezing bottleneck design for compact convolutional neural networks model*. Image and Vision Computing, 2019. **89**: p. 276-288.
- [29] Mattos, A.B., et al. *Assessing texture descriptors for seismic image retrieval*. IEEE.
- [30] Van Wagoner, J.C., et al., *Seismic stratigraphy interpretation using sequence stratigraphy: Part 2: key definitions of sequence stratigraphy*. 1987.
- [31] Baroni, L.a.S., Reinaldo Mozart and Ferreira, Rodrigo and Chevitere, Daniel and Szwarcman, Daniela and Brazil, Emilio Vital, *Penobscot Interpretation Dataset*. 2018.
- [32] Vail, P.R., R.M. Mitchum Jr, and S. Thompson Iii, *Seismic stratigraphy and global changes of sea level: Part 4. Global cycles of relative changes of sea level.: Section 2. Application of seismic reflection configuration to stratigraphic interpretation*. 1977.
- [33] Posamentier, H.W. and P.R. Vail, *Eustatic controls on clastic deposition II—sequence and systems tract models*. 1988.
- [34] Reading, H.G. and M. Richards, *Turbidite systems in deep-water basin margins classified by grain size and feeder system*. AAPG bulletin, 1994. **78**(5): p. 792-822.
- [35] Knebel, H.J., *Holocene depositional history of a large glaciated estuary, Penobscot Bay, Maine*. Marine Geology, 1986. **73**(3-4): p. 215-236.
- [36] de Winter, J.C.F., S.D. Gosling, and J. Potter, *Comparing the Pearson and Spearman correlation coefficients across distributions and sample sizes: A tutorial using simulations and empirical data*. Psychological methods, 2016. **21**(3): p. 273.
- [37] Kingma, D.P. and J.L. Ba. *Adam: A method for stochastic gradient descent*.
- [38] Ruder, S., *An overview of gradient descent optimization algorithms*. arXiv preprint arXiv:1609.04747, 2016.
- [39] Ding, L., J. Zhang, and L. Bruzzone, *Semantic Segmentation of Large-Size VHR Remote Sensing Images Using a Two-Stage Multiscale Training Architecture*. IEEE Transactions on Geoscience and Remote Sensing, 2020.
- [40] Liu, M.-Y. and O. Tuzel. *Coupled generative adversarial networks*. 2016.
- [41] Yoo, D., et al. *Pixel-level domain transfer*. 2016. Springer.

# Supplementary Section

Supplementary Table 1. Layerwise architectural description of the feature maps for the source and target domains for 4 encoders followed by a gap layer and 2 FC layers ( $4RB+GAP+2FC$ )

Entity	Entity Size	Entity Description
<i>first_conv_source</i>	(128, 64, 40, 40)	SD image batch feature map after first conv layer
<i>first_conv_target</i>	(128, 64, 40, 40)	TD image batch feature map after first conv layer
<i>rb_1_source</i>	(128, 64, 20, 20)	SD image batch feature map after first RB
<i>rb_1_target</i>	(128, 64, 20, 20)	TD image batch feature map after first RB
<i>rb_2_source</i>	(128, 128, 10, 10)	SD image batch feature map after second RB
<i>rb_2_target</i>	(128, 128, 10, 10)	TD image batch feature map after second RB
<i>rb_3_source</i>	(128, 256, 5, 5)	SD image batch feature map after third RB
<i>rb_3_target</i>	(128, 256, 5, 5)	TD image batch feature map after third RB
<i>rb_4_source</i>	(128, 512, 3, 3)	SD image batch feature map after fourth RB
<i>rb_4_target</i>	(128, 512, 3, 3)	TD image batch feature map after fourth RB
<i>gap_source</i>	(128, 512, 1, 1)	SD image batch feature map after GAP layer
<i>gap_target</i>	(128, 512, 1, 1)	TD image batch feature map after GAP layer
<i>fc1_source</i>	(128, 256)	SD image batch feature map after first FC layer
<i>fc1_target</i>	(128, 256)	TD image batch feature map after first FC layer
<i>fc_last_source</i>	(128, 3)	SD image batch output after lastFC layer
<i>fc_last_target</i>	(128, 3)	TD image batch output after lastFC layer

Supplementary Table 2. Layerwise architectural description of the feature maps for the source and target domains for 3 encoders followed by a gap layer and 2 fc layers ( $3RB+GAP+2FC$ )

Entity	Entity Size	Entity Description
<i>first_conv_source</i>	(128, 64, 40, 40)	SD image batch feature map after first conv layer
<i>first_conv_target</i>	(128, 64, 40, 40)	TD image batch feature map after first conv layer
<i>rb_1_source</i>	(128, 64, 20, 20)	SD image batch feature map after first RB
<i>rb_1_target</i>	(128, 64, 20, 20)	TD image batch feature map after first RB
<i>rb_2_source</i>	(128, 128, 10, 10)	SD image batch feature map after second RB
<i>rb_2_target</i>	(128, 128, 10, 10)	TD image batch feature map after second RB
<i>rb_3_source</i>	(128, 256, 5, 5)	SD image batch feature map after third RB
<i>rb_3_target</i>	(128, 256, 5, 5)	TD image batch feature map after third RB
<i>gap_source</i>	(128, 256, 1, 1)	SD image batch feature map after GAP layer
<i>gap_target</i>	(128, 256, 1, 1)	TD image batch feature map after GAP layer
<i>fc1_source</i>	(128, 128)	SD image batch feature map after first FC layer
<i>fc1_target</i>	(128, 128)	TD image batch feature map after first FC layer
<i>fc_last_source</i>	(128, 3)	SD image batch output after lastFC layer
<i>fc_last_target</i>	(128, 3)	TD image batch output after lastFC layer

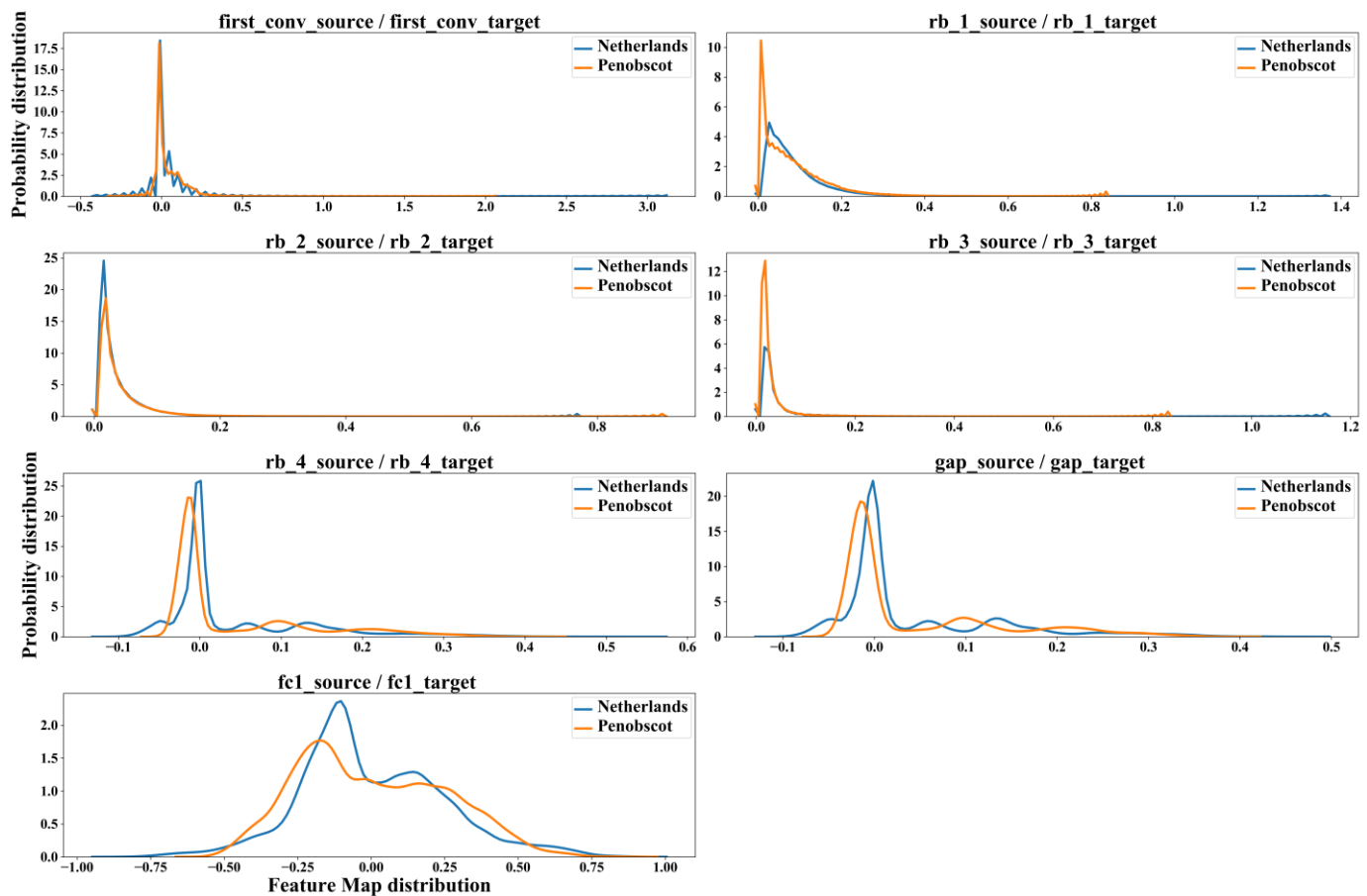
Supplementary Table 3. Statistical variants for  $4RB+GAP+2FC$  architecture. Pearson coefficient and p-value determine how well DDA model perform.

Entity	Pearson Coefficient	p-value
<i>first_conv_source - first_conv_target</i>	0.03	0.00
<i>rb_1_source - rb_1_target</i>	0.08	0.00
<i>rb_2_source - rb_2_target</i>	0.23	0.00
<i>rb_3_source - rb_3_target</i>	0.52	0.00
<i>rb_4_source - rb_4_target</i>	-0.03	0.00
<i>gap_source - gap_target</i>	-0.03	0.00
<i>fc1_source - fc1_target</i>	-0.07	0.00

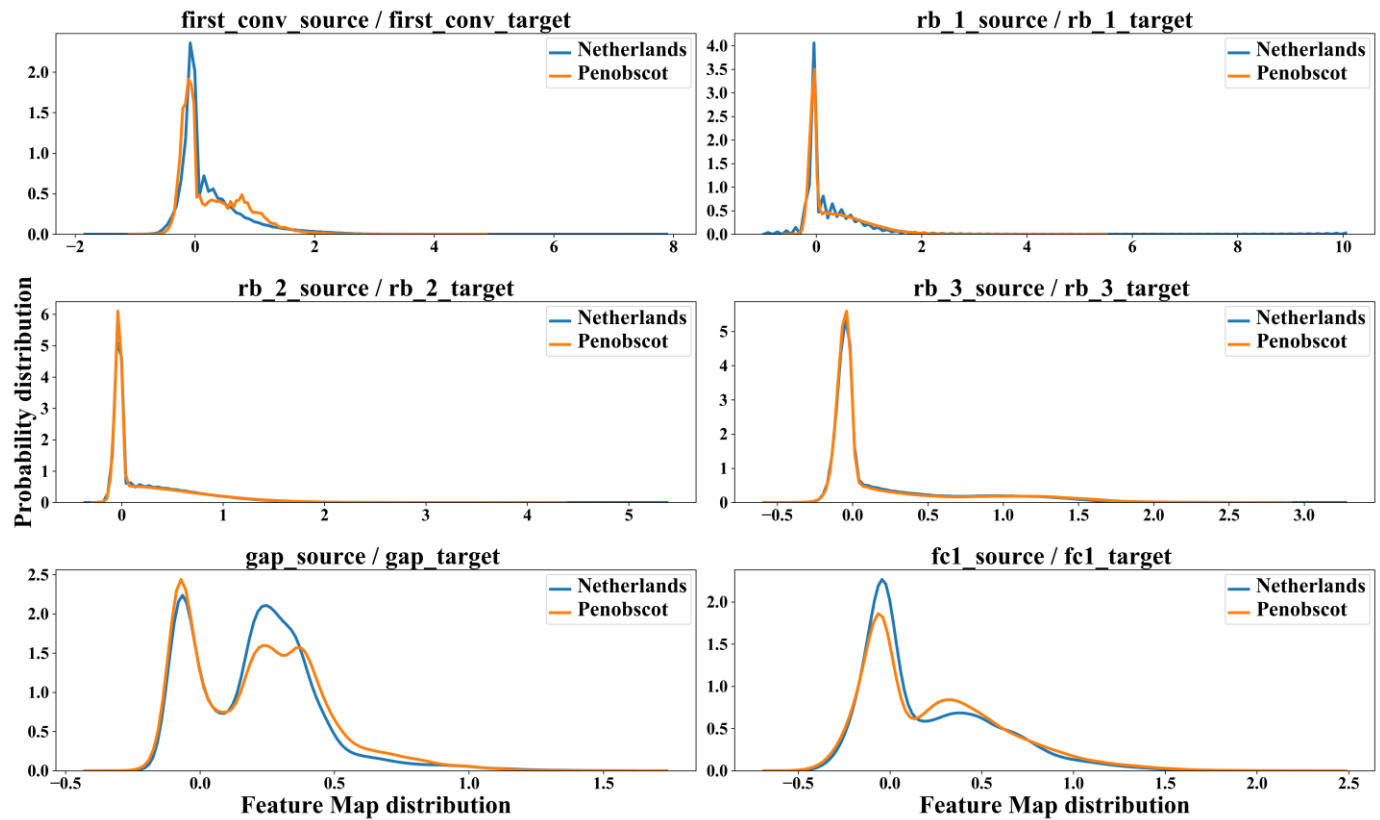


Supplementary Table 4. Statistical variants for  $3RB+GAP+2FC$  architecture. Pearson coefficient and p-value determine how well DDA model perform.

Entity	Pearson Coefficient	p-value
$first\_conv\_source - first\_conv\_target$	0.00	0.00
$rb\_1\_source - rb\_1\_target$	0.05	0.00
$rb\_2\_source - rb\_2\_target$	0.15	0.00
$rb\_3\_source - rb\_3\_target$	0.62	0.00
$gap\_source - gap\_target$	0.25	0.00
$fc1\_source - fc1\_target$	0.11	0.00



Supplementary Figure 1. Comparison of the feature maps distributions from source and target domains. Distributions from the layer for the architecture with 4 Encoders followed by a GAP layer and 2 FC layers ( $4RB+GAP+2FC$ ) shows how the SD (Netherlands) and TD (Canada) distributions correlate.



Supplementary Figure 2. Comparison of the feature maps distributions from source and target domains. Distributions from the layer for the architecture with 3 Encoders followed by a GAP layer and 2 FC layers ( $3RB+GAP+2FC$ ) shows how the SD (Netherlands) and TD (Canada) distributions correlate.